electronics

MDPI

Article

Experimental Study of Joint Hierarchical Equalization Scheme for AF/DF Relaying in a 1 Gbps Underwater Visible Light Communication System

Zhilan Lu [1,2,3], Fujie Li [1], Fang Dong [1], Zengyi Xu [1], Ziwei Li [1], Feng Bao [1], Chao Shen [1], Junwen Zhang [1] and Nan Chi [1,*]

[1] Key Laboratory for the Information Science of Electromagnetic Waves (MoE), College of Future Information Technology, Fudan University, Shanghai 200433, China; chaoshen@fudan.edu.cn (C.S.)
[2] Shanghai Engineering Research Center of Low-Earth-Orbit Satellite Communication and Applications, Shanghai 200433, China
[3] Shanghai Collaborative Innovation Center of Low-Earth-Orbit Satellite Communication Technology, Shanghai 200433, China
* Correspondence: nanchi@fudan.edu.cn

Abstract

To overcome limitations imposed by device bandwidth and transmission range in underwater visible light communication (UVLC) systems, this study compares amplify-and-forward (AF) and decode-and-forward (DF) relaying on a relay-assisted UVLC (RA-UVLC) experimental platform. A joint hierarchical equalization scheme (JHES) is proposed, comprising two branches tailored to the different transmission characteristics of AF and DF. For the AF scheme, lightweight cascaded spectral pre-equalization (LCS-PE) performs two-stage spectral compensation to suppress spectral distortion across successive hops. For the DF scheme, hierarchical multi-domain post-equalization (HMD-PE) successively compensates for distortion in the frequency, time, and symbol domains. A 5 m water tank and neutral density filters are used to establish attenuation-equivalent transmission conditions. Experimental results show that both schemes achieve transmission at 1 Gbps over an attenuation-equivalent distance of 1 km, with an end-to-end bit error rate below 3.8×10^{-3}. Their performance is further compared under four disturbance conditions. These results provide experimental evidence for selecting equalization methods and relay schemes in multi-hop UVLC systems.

Keywords: underwater visible light communication; relay-assisted underwater visible light communication; multi-hop underwater network; hierarchical equalization

Check for updates

Academic Editor: Jiun-Haw Lee

Received: 25 September 2026
Revised: 9 November 2026
Accepted: 11 November 2026
Published: 13 November 2026

Copyright: © 2026 by the authors. Licensee MDPI, Basel, Switzerland. This article is an open access article distributed under the terms and conditions of the Creative Commons Attribution (CC BY) license.

1. Introduction

Sixth-generation mobile communication (6G) [1,2] systems aim to establish high-capacity space–air–ground–sea integrated networks capable of supporting the growing demand for ultra-high-throughput and low-latency data transmission in emerging applications, including artificial intelligence, large-scale model training, edge computing, and optical interconnects in data centers [3,4]. With the rapid expansion of wireless services, conventional microwave bands are experiencing severe spectrum congestion, which constrains further improvements in system capacity. To address this limitation, 6G advocates full-spectrum access, promoting the utilization of higher-frequency bands such as millimeter-wave, terahertz, and visible light to exploit abundant spectral resources [5,6]. In underwater communication scenarios, the characteristics of the propagation medium play a decisive role in system performance. Seawater exhibits strong absorption and attenuation

of electromagnetic waves, posing a fundamental challenge for underwater wireless communication. Notably, the blue-green region of the visible spectrum coincides with the optical transmission window in seawater. Owing to its relatively low attenuation, inherent security, resistance to electromagnetic interference, and high signal-to-noise ratio (SNR), this spectral band is suited for high-speed underwater wireless transmission [7,8]. Consequently, underwater visible light communication (UVLC) has emerged as a promising technology for high-capacity underwater communication networks. Recent studies have demonstrated that visible light communication (VLC) can achieve gigahertz-level transmission bandwidths at a single wavelength [9,10], offering data rates several orders of magnitude higher than those of conventional underwater acoustic communication (UAC) [11]. Moreover, unlike radio frequency (RF) communication, UVLC is not constrained by the skin effect in conductive media, further highlighting its advantages in underwater environments [7].

However, device-level constraints remain a primary bottleneck in the advancement of VLC. Owing to the absence of mature optical amplification technologies in the visible spectrum, overall system performance largely depends on the output power of the transmitter laser and the responsivity and sensitivity of the photodetector at the receiver. As a result, the transmission range of current VLC systems is typically restricted to several hundred meters [12,13]. With increasing link distance, channel fading and cumulative noise further reduce the SNR, thereby limiting the achievable data rate. Relay-assisted UVLC (RA-UVLC) offers an approach to improving transmission performance without relying on optical amplification, thereby extending the communication range and broadening its potential applications. Figure 1 depicts a representative underwater visible light multi-hop relay network architecture. In this configuration, underwater sensor nodes forward data to surface buoys or surface ships through multiple autonomous underwater vehicles (AUVs) and remotely operated vehicles (ROVs) acting as relay nodes. VLC links are employed for underwater transmission, while buoys or ships subsequently forward the received information to shore-based access points or base stations using radio frequency or free-space optical (FSO) links.

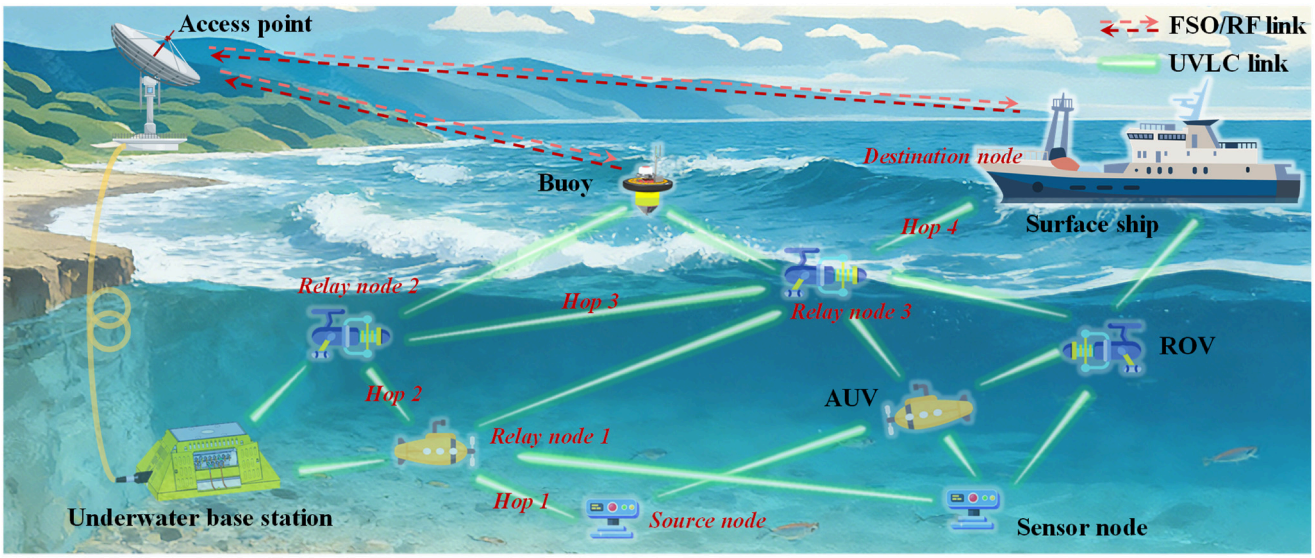

Figure 1. Scenario of relay-assisted underwater visible light network.

Table 1 summarizes representative simulation and experimental studies on RA-UVLC systems [14–18]. Most RA-UVLC studies have been limited to simulations, with relatively few experimental demonstrations. In 2016, Jamali et al. analyzed underwater relay scenarios based on optical code-division multiple access (OCDMA), deriving bit error rate (BER)

expressions for both uplink and downlink transmissions [14]. Their simulation results verified that multi-hop relaying can effectively extend communication distance, demonstrating the feasibility of achieving 100 Mbps transmission over 90 m using a two-hop configuration [14]. In 2023, Luo et al. proposed an optimized real-time video transmission scheme for underwater optical links established by AUVs [16]. To address dynamic underwater conditions and interference, they introduced an adaptive beam-steering and power-control algorithm to enhance link robustness. Simulations indicated reliable communication below 10 Mbps over distances shorter than 1 km. In the same year, Jiang et al. investigated the outage performance of an RA-UVLC system under a weak turbulence model, reporting simulated 1 Gbps transmission over 40 m with one to four relay nodes, corresponding to two to five hops [17]. More recently, in 2024, Salman et al. experimentally demonstrated an RA-UVLC system using multiple optical receivers, signal-combining techniques, and a channel-aware algorithm, reporting 0.2 Mbps transmission over a 7.5 m link in water with a turbidity of 25 NTU, achieving a packet success rate of approximately 68% [18]. Overall, practical implementations of visible light relay systems remain at an early stage, with only a limited number of reported studies. Moreover, most existing models and experiments rely on light-emitting diodes (LEDs), which are inherently constrained by limited modulation bandwidth, relatively low output power, and large beam divergence. Transitioning to laser diode (LD)-based underwater visible light relay systems offers significant potential for improving bandwidth, power efficiency, and transmission distance.

Table 1. Performance and technical solutions of recent RA-UVLC systems.

Ref.	Year	Simulation/ Experiment	System	Source	Data Rate	Distance	Number of Hops
[14]	2016	Simulation	UVLC	LED or LD	100 Mbps	90 m	2
[15]	2021	Simulation	RF + UVLC	LD	<500 kbps	<100 m	2
[16]	2023	Simulation	UVLC	LED	<10 Mbps	<1 km	2
[17]	2023	Simulation	UVLC	LD	1 Gbps	40 m	2~5
[18]	2024	Experiment	UVLC	LED	200 kbps	7.5 m	2
This work	2026	Experiment	UVLC	LD	1 Gbps	1 km (attenuation-equivalent)	5

In this study, we experimentally implement an RA-UVLC system supporting amplify-and-forward (AF) and decode-and-forward (DF) strategies, using a green laser as the optical source. A 5 m water tank with calibrated optical attenuators is used to define attenuation-equivalent distances. Multi-hop transmission is implemented through sequential acquisition, processing, and replay using the same set of equipment. To increase channel diversity and alleviate the impact of scattering and absorption in water, the circularly polarized transmission, dual-aperture reception, and polarization diversity architecture [19] from our previous work is adopted. To enhance system robustness and compensate for signal distortion arising from limited high-frequency response, a joint hierarchical equalization scheme (JHES) is proposed for the AF and DF schemes. For the AF scheme, a lightweight cascaded spectral pre-equalization (LCS-PE) approach is adopted to compensate for the cascaded high-frequency roll-off while maintaining low processing complexity. For the DF scheme, a hierarchical multi-domain post-equalization (HMD-PE) strategy is employed. By cascading equalization across the frequency, time, and symbol domains, the approach enables enhanced compensation of channel distortions. Experimental results demonstrate the feasibility of achieving 1 Gbps transmission over an equivalent 1 km underwater link using relay assistance. Finally, performance under water pump-induced disturbances and different salinity conditions is evaluated to further assess the feasibility of the proposed schemes.

2. Setup and Principle of the RA-UVLC System

2.1. The Proposed Joint Hierarchical Equalization Scheme

Figure 2 illustrates the proposed joint hierarchical equalization scheme, with the lightweight cascaded spectral pre-equalization scheme shown in Figure 2a. LCS-PE can be implemented using two cascaded analog pre-equalization circuits [20,21]. In this experiment, the frequency responses are calculated from the resistance, inductance, and capacitance parameters of the circuits, and cascaded pre-equalization is emulated in the digital domain. Multiplication of the received signal spectrum by these frequency responses emulates the equalization process within an AF relay. Conventional pre-equalization typically applies pre-emphasis to high-frequency components to compensate for bandwidth limitations [19,22]. However, in the present system, mid-frequency components also contribute significantly to overall performance. If the center frequency of the Zobel network were set only near the highest operating frequency (500 MHz), the mid-frequency components would experience progressive attenuation after multiple relay stages. To address this issue, a cascaded spectral pre-equalization strategy is adopted. The first stage enhances the mid-frequency band (centered at 250 MHz), while the second stage emphasizes the high-frequency band (centered at 500 MHz). This design not only compensates for frequency-selective fading but also prevents excessive amplification of resonance peaks across multiple hops. The frequency response of the Zobel-based pre-equalization network is determined by the circuit parameters, including resistance, capacitance, and inductance. These parameters can be equivalently expressed in terms of the design center frequency f_0, the maximum attenuation factor A_m, and the characteristic frequency f_h corresponding to an attenuation level of $A_m/2$. As shown in Figure 2a, pre-equalization Curve 1 is configured with $f_0 = 250$ MHz, $A_m = 5$ dB , $f_h = 550$ MHz, whereas Curve 2 adopts $f_0 = 500$ MHz, $A_m = 5$ dB, $f_h = 550$ MHz. The corresponding spectral responses are denoted by $H_{C1}(k)$ and $H_{C2}(k)$, respectively. Let $y(n)$ represent the received signal. After spectrum-slicing pre-equalization, the processed signal $\hat{x}(n)$ can be expressed as

$$\hat{x}(n) = \mathcal{F}^{-1}\{\mathcal{F}\{y(n)\}\cdot H_{C1}(k)\cdot H_{C2}(k)\}, \quad (1)$$

where $\mathcal{F}\{\cdot\}$ and $\mathcal{F}^{-1}\{\cdot\}$ denote the Fourier transform and inverse Fourier transform, respectively. The parameters of the two stages are selected according to the transmitter and receiver devices and the frequency response of the current link. After LCS-PE, each signal is normalized, and the transmit peak-to-peak voltage is set to the value corresponding to the system's optimal operating point. This compensates for the overall amplitude changes introduced by LCS-PE while preserving the relative amplitudes of the different frequency components. With the detector and receiver circuit settings unchanged, these equalization parameters do not directly alter the detector's intrinsic dynamic range. Their effect on link performance primarily arises from the spectral shaping of the transmitted signal.

Figure 2b illustrates the principle of the HMD-PE scheme. For signals captured by the dual-polarization receiver, hierarchical multi-domain post-equalization is performed to recover symbol-level signals. The two signals are then fused via an SNR-weighted combining scheme, followed by re-modulation to generate the transmit waveform for the subsequent hop.

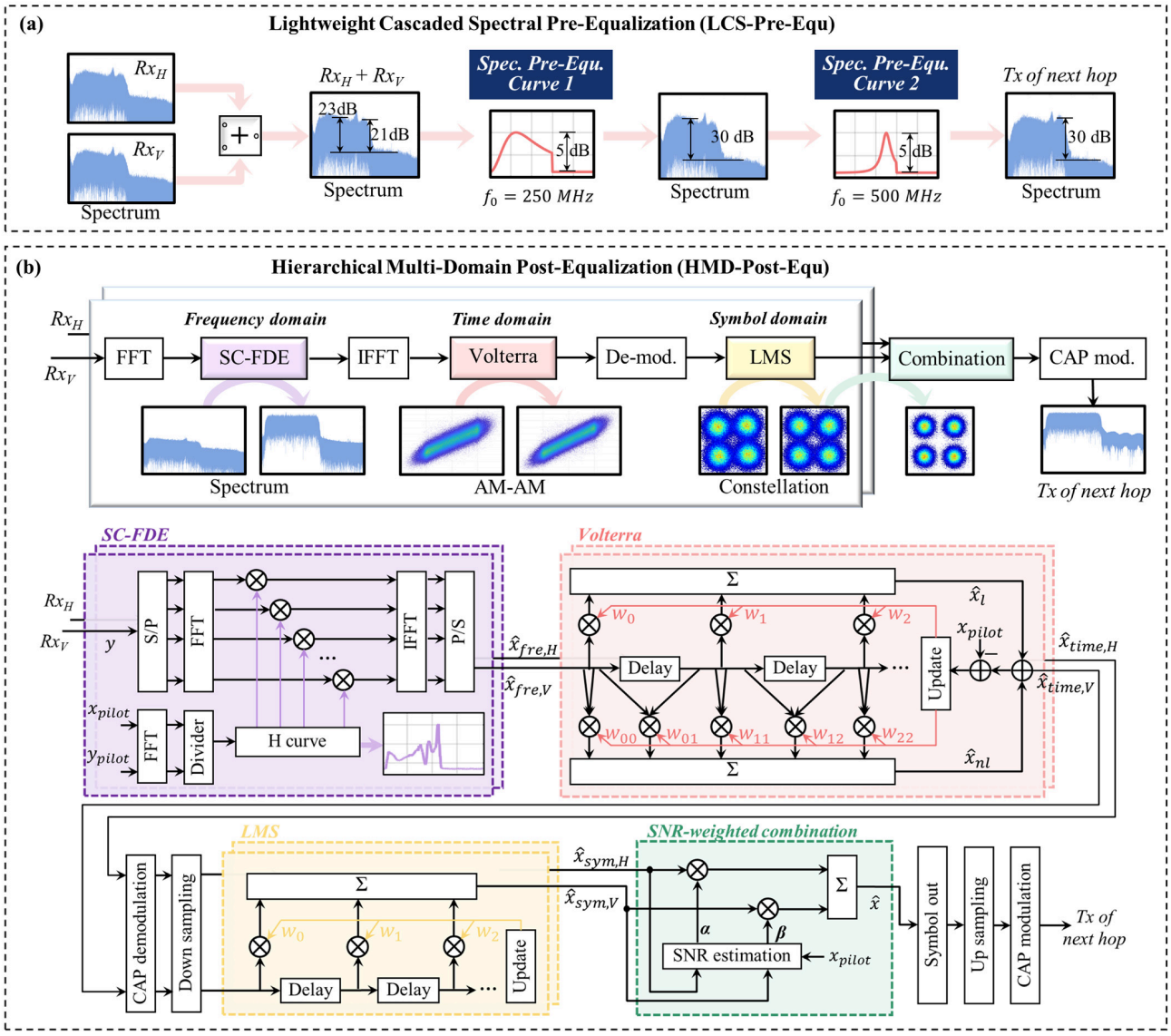

Figure 2. Principles of the proposed joint hierarchical equalization scheme. Principles of the (**a**) lightweight cascaded spectral pre-equalization scheme and (**b**) hierarchical multi-domain post-equalization strategy.

Channel estimation [23] is important for compensating for signal distortion in VLC systems. In this experiment, frequency-domain compensation is implemented using a single-carrier frequency-domain equalization (SC-FDE) algorithm. For each polarization branch, the transmitted training blocks and the corresponding received blocks are transformed using fast Fourier transform (FFT). The transmitted pilot spectrum is divided directly by the received pilot spectrum at every FFT bin. No denominator floor, regularization, gain clipping, or frequency-bin mask is applied in the spectral division. Therefore, a small received-pilot spectral magnitude can produce a large coefficient estimate. In this experiment, smoothing is used to reduce local fluctuations in the coefficient estimates. The complex ratios are first averaged across training blocks and then smoothed along frequency to obtain the equalization coefficient vector. This vector is applied to all received blocks in the captured frame. The coefficient estimation and equalization are expressed as follows:

$$G(k) = \mathcal{S}_W\left\{\frac{1}{M}\sum_{m=1}^{M}\frac{X_{pilot,m}(k)}{Y_{pilot,m}(k)}\right\}, \quad \hat{x}_{fre}(n) = \mathcal{F}^{-1}[\mathrm{Y}(k)\mathrm{G}(k)]. \tag{2}$$

where k is the FFT-bin index, and m indexes the M training blocks. $X_{pilot,m}(k)$ and $Y_{pilot,m}(k)$ are the transmitted and received pilot spectra, respectively. $\mathcal{S}_W$ denotes smoothing along frequency with span parameter W. After optimization, the smoothing span parameter W and the number of training blocks M were set to 32 and 40, respectively. $Y(k)$ denotes the spectrum of a received block. The resulting samples $\hat{x}_{fre}(n)$ form the input to time-domain equalization.

Time-domain equalization is carried out using a Volterra-filter-based structure combined with a least mean square (LMS) algorithm, enabling compensation for both linear and nonlinear distortions. The linear and nonlinear components are denoted by $\hat{x}_l(n)$ and $\hat{x}_{nl}(n)$, respectively. The overall time-domain equalized output is denoted by $\hat{x}_{time}(n)$:

$$\hat{x}_l(n) = \sum_{m=0}^{N_l-1} w_m \hat{x}_{fre}(n-m), \tag{3}$$

$$\hat{x}_{nl}(n) = \sum_{m_1=0}^{N_{nl}-1} \sum_{m_2=m_1}^{N_{nl}-1} w_{m_1 m_2} \hat{x}_{fre}(n-m_1)\hat{x}_{fre}(n-m_2), \tag{4}$$

$$\hat{x}_{time}(n) = \hat{x}_l(n) + \hat{x}_{nl}(n). \tag{5}$$

N_l and N_{nl} denote the numbers of taps of the linear and nonlinear components. In this experiment, the optimized values are 21 and 23, respectively.

After demodulation and down-sampling, symbol-level outputs are obtained. Symbol-domain equalization is then performed using a 41-tap LMS-based linear equalizer as described by (3), primarily to mitigate inter-symbol interference (ISI). The symbols obtained after HMD-PE processing for the two polarization branches are denoted by $\hat{x}_{sym,V}(n)$ and $\hat{x}_{sym,H}(n)$.

An SNR-weighted scheme is used to combine the two signals. The SNR of each branch is first estimated from its pilot sequence using (6). The estimated SNR values are used to determine the weighting coefficients α and β for combining the two signals. The propagation paths of the two branches partially overlap and may therefore be affected by correlated noise. However, (6) estimates the SNR of each branch separately and uses these estimates as the weights in the summation, without requiring the two branches to be uncorrelated.

$$\alpha = \frac{\sum_{n=1}^{N_p} \left|x_{pilot}(n)\right|^2}{\sum_{n=1}^{N_p} \left|x_{pilot}(n) - \hat{x}_{sym,H}(n)\right|^2}, \quad \beta = \frac{\sum_{n=1}^{N_p} \left|x_{pilot}(n)\right|^2}{\sum_{n=1}^{N_p} \left|x_{pilot}(n) - \hat{x}_{sym,V}(n)\right|^2}. \tag{6}$$

N_p is the number of pilot symbols. Through weighted summation, the final recovered symbols $\hat{x}(n)$ are obtained:

$$\hat{x}(n) = \frac{\alpha \hat{x}_{sym,H}(n) + \beta \hat{x}_{sym,V}(n)}{\alpha + \beta}. \tag{7}$$

The equalization parameters are optimized using a set of captured signals at the optimal transmitter operating point, including the pilot lengths for SC-FDE and SNR estimation, the SC-FDE smoothing span, and the numbers of taps in the Volterra and symbol-domain LMS equalizers. Once determined, these design settings are kept fixed in the subsequent transmission and disturbance tests. The SC-FDE coefficient vector is estimated separately from the received pilots in each captured frame, and the LMS coefficients are updated during training. In the ablation experiments, only the equalizer under investigation is removed, while the remaining configuration is unchanged.

2.2. Channel and System Model

In underwater environments, visible light propagation is primarily affected by absorption, scattering, and turbulence. In the absence of turbulence, underwater optical propagation follows an exponential attenuation law [24]. For an attenuation-equivalent

transmission distance L, the relationship between the received optical power P_{rx} and transmitted optical power P_{tx} is expressed as

$$P_{rx}/P_{tx} = \exp\left[-\gamma_{ref}(\lambda)L\right]. \tag{8}$$

Here, γ_{ref} is the reference diffuse attenuation coefficient [24]. The experimental wavelength is 520 nm, and equivalent distances are calculated for Jerlov type-I water. Linear interpolation between the values at 500 nm and 525 nm in [24] gives an estimated coefficient at 520 nm that is slightly lower than the value at 525 nm. To provide a conservative estimate of the equivalent distance, the diffuse attenuation coefficient at 525 nm ($0.0398\ \mathrm{m}^{-1}$) is used in this work. At the experimental wavelength of 520 nm, the filter is adjusted at each hop to match the target received optical power.

In the RA-UVLC system, an N-hop link contains $(N-1)$ relay nodes. Within the linear operating range, each hop can be modeled as

$$Y_n(k) = H_n(k)X_n(k) + N_n(k), \tag{9}$$

where $X_n(k)$ and $Y_n(k)$ denote the transmitted and received spectra at the nth hop, respectively. $H_n(k)$ is the equivalent electrical frequency response incorporating the device and propagation responses, and $N_n(k)$ is the equivalent noise at the receiver output of that hop. For the AF scheme, after N hops, the overall channel response and accumulated noise are denoted by $H_{total}(k)$ and $N_{total}(k)$, respectively, yielding

$$Y_N(k) = H_{total}(k)X_1(k) + N_{total}(k). \tag{10}$$

For the AF scheme, the actual gain or amplitude normalization and the two-stage pre-equalization response at each relay are included in the cascade. The transmit signal for the next hop, overall response, and accumulated noise are then expressed as

$$A_n(k) = G_nC_n(k), \quad X_{n+1}(k) = A_n(k)Y_n(k), \tag{11}$$

$$H_{total}(k) = \prod_{n=1}^{N} H_n(k) \quad \prod_{n=1}^{N-1} A_n(k), \tag{12}$$

$$N_{total}(k) = \sum_{i=1}^{N}\left[\prod_{n=i+1}^{N} H_n(k)A_{n-1}(k)\right]N_i(k). \tag{13}$$

Here, G denotes the actual gain or amplitude normalization coefficient, C denotes the cascaded response of the two pre-equalization stages, and A is their product. The subscript identifies the corresponding relay hop. Noise introduced at preceding hops continues to propagate through the subsequent transmission, filtering, and gain stages.

For the DF scheme, impairment propagation differs from the linear noise accumulation represented by $N_{total}(k)$ in (10)–(13). Each relay reconstructs the transmit signal through equalization, combining, decisions, and remodulation. Consequently, analog noise from preceding hops is not directly forwarded and successively weighted by the subsequent channel responses. However, incorrect decisions at a relay may be carried into the regenerated transmit signal. Specifically, $X_n(k)$ in (9) is the spectrum of the waveform regenerated from the bit sequence detected at the preceding relay and may therefore reflect decision errors introduced at earlier hops. These errors affect subsequent transmission through the regenerated signal, rather than through a linear cascade of the channel responses $H_n(k)$. Accordingly, the DF process is modeled by recursively updating the detected bit sequence and the regenerated waveform. With the source bit sequence as the initial input, the per-hop processing and end-to-end BER are expressed as

$$\hat{b}_n = D_n\{E_n[y_n]\}, \quad x_{n+1} = M_n\left(\hat{b}_n\right), \tag{14}$$

$$BER = \frac{1}{B}\sum_{q=1}^{B} I\{\hat{b}_N[q] \neq b_{tx}[q]\}. \quad (15)$$

Here, E denotes synchronization, equalization, and dual-branch combining; D denotes decisions and demapping; M denotes remodulation; $I\{\cdot\}$ is the indicator function; B is the number of valid data bits included in the final aligned comparison; and b denotes a bit sequence. DF relays do not perform per-hop forward error correction (FEC) decoding. Decision errors introduced at intermediate relays may propagate through subsequent regeneration stages. The end-to-end BER is therefore calculated by comparing the final detected bit sequence with the original source bit sequence b_{tx}.

In intensity-modulation and direct-detection visible light communication systems, the channel response $H_n(k)$ typically exhibits a low-pass characteristic. Consequently, under the AF strategy, high-frequency components are progressively attenuated with increasing hop count due to the multiplicative nature of the channel response. In contrast, the DF strategy effectively mitigates this attenuation through signal regeneration at each relay.

2.3. Experimental Setup

Figure 3 illustrates the experimental configuration of the RA-UVLC system, which comprises a source node, a relay node, a destination node, and the underwater channel. The actual water-tank path and photographs of the experimental setup are shown in Figure 3c–f.

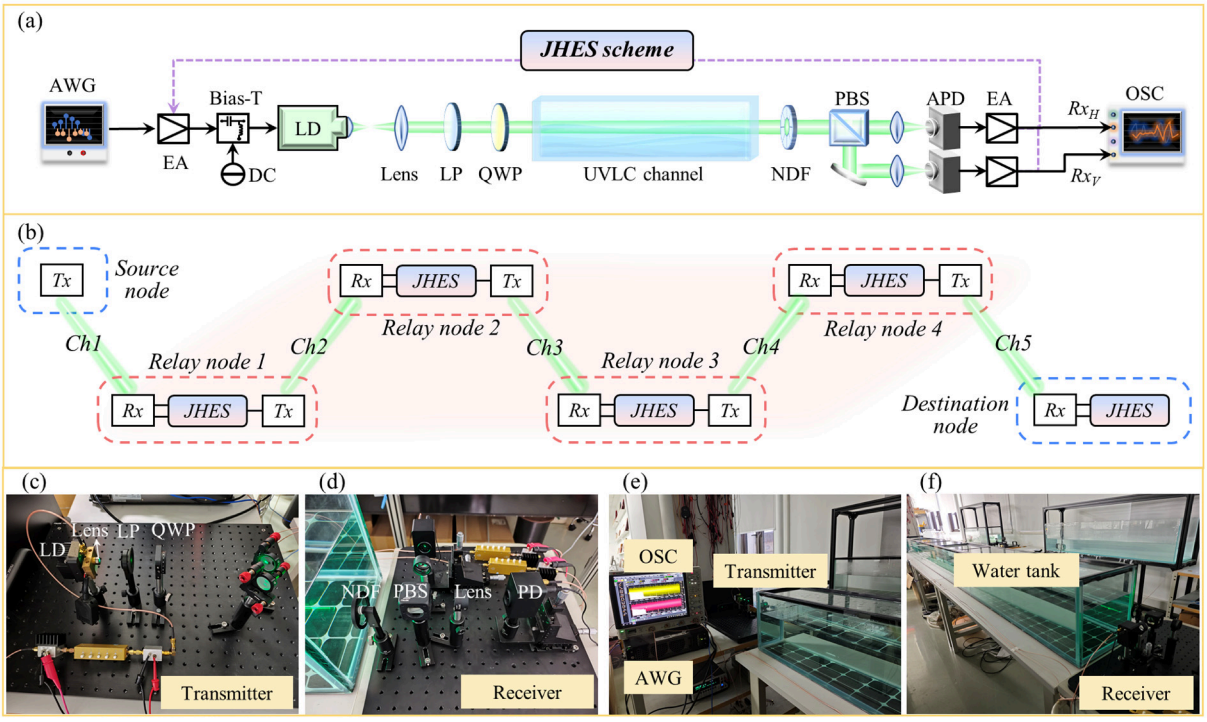

Figure 3. Experimental setup of the RA-UVLC system: (**a**) transmitter, receiver, and signal processing; (**b**) five-hop node configuration; (**c**) transmitter; (**d**) receiver; and (**e**,**f**) photographs of the water tank and transceivers.

At the source node, a pseudo-random bit sequence is mapped to complex QAM-4 constellation symbols and then up-sampled at four samples per symbol. The symbol rate is 500 MBaud, corresponding to a bit rate of 1 Gbps. Because directly modulated visible light systems can transmit only real-valued signals, carrier-less amplitude and phase (CAP) modulation is employed to generate the real-valued transmit waveform, with a pulse-shaping roll-off factor of 0.105. The resulting signal is uploaded to an arbitrary waveform generator (AWG, M8190A, Keysight, Santa Rosa, CA, USA) to generate the corresponding

electrical waveform. The AWG supports a maximum sampling rate of 12 GSa/s and operates at a sampling rate of 2 GSa/s in this experiment. The electrical signal is subsequently amplified by an electrical amplifier (EA, ZHL-1042J+, Mini-Circuits, Brooklyn, NY, USA) and fed into a bias-tee (JEBT-4R2GW+, Mini-Circuits, Brooklyn, NY, USA). Combined with a direct current (DC), the signal drives the LD to emit modulated optical output. The emitted beam is collimated using a lens assembly, linearly polarized by a linear polarizer (LP), and converted into circular polarization through a quarter-wave plate (QWP).

The circularly polarized beam propagates through a 5 m water tank to emulate the underwater channel. A neutral density filter (NDF) positioned at the tank exit provides controllable attenuation to simulate extended transmission distances, which has been widely used in previous underwater optical communication studies [25]. The transmitted optical power is measured before the beam enters the water tank. At each hop, the NDF is adjusted so that the total received optical power measured immediately before the polarization beam splitter (PBS) matches the value corresponding to the target equivalent distance. The beam then enters the PBS, which separates it into horizontal and vertical polarization components. Each component is focused by a lens onto an avalanche photodetector (APD). The detected electrical signals are amplified and subsequently forwarded to the relay node for further processing.

At the relay node, different processing schemes are implemented for the AF and DF strategies. For the AF scheme, the two electrical signals obtained from the APDs are first combined. To compensate for high-frequency fading, the combined signal is processed using LCS-PE before driving the laser for the next hop. For the DF scheme, the two signals detected by the APDs are captured using a high-speed oscilloscope (OSC, MSO9404A, 20 GSa/s, Keysight) and subsequently processed offline. The received waveforms undergo frequency-domain and time-domain equalization, demodulation, symbol-domain equalization, and signal combining. Decisions are made on the combined symbols, and the detected data are re-modulated to generate the transmit waveform for the next hop. For both strategies, the processed waveform from each hop is loaded into the AWG to drive the LD, and the emitted beam again passes through the water tank and NDF. This procedure is repeated to complete multi-hop transmission. After multiple hops, the signal reaches the destination node. The final BER is calculated relative to the original transmitted data, and DF does not perform per-hop FEC decoding. The key experimental parameters are summarized in Table 2.

Table 2. Detailed experimental system parameters.

Parameter		Symbol	Value
Transmitter	Output power	P_{tx}	19 dBm
	Wavelength	λ	520 nm
	Linewidth	$\Delta\lambda$	~3.3 nm
	Luminous flux	Φ	41.24 lm
Modulation	Symbol rate	R_S	500 MBaud
	Modulation format	/	QAM-4
	Up-sampling rate	/	4 samples per symbol
	Roll-off factor	/	0.105
Channel	Attenuation factor	γ_{ref}	0.0398 m^{-1} (Jerlov I)
	Temperature	T	300 K
Receiver	Photosensitive area diameter	/	~200 μm
	Receiver aperture diameter	/	25.4 mm

3. Experimental Results

To determine the optimal operating point, a discrete multi-tone (DMT) signal with bit and power loading [26,27] was first transmitted in a back-to-back (B2B) configuration. The achievable information rate (AIR) was evaluated as a function of bias current and peak-to-peak driving voltage (Vpp), as presented in Figure 4a. Both excessively high and excessively low values of Vpp and bias current degrade system performance. High values of Vpp or bias current introduce nonlinear distortion, whereas low values result in limited SNR, insufficient modulation depth, and increased BER. Based on the experimental results, the optimal operating point was identified at a Vpp of 550 mV and a bias current of 60 mA.

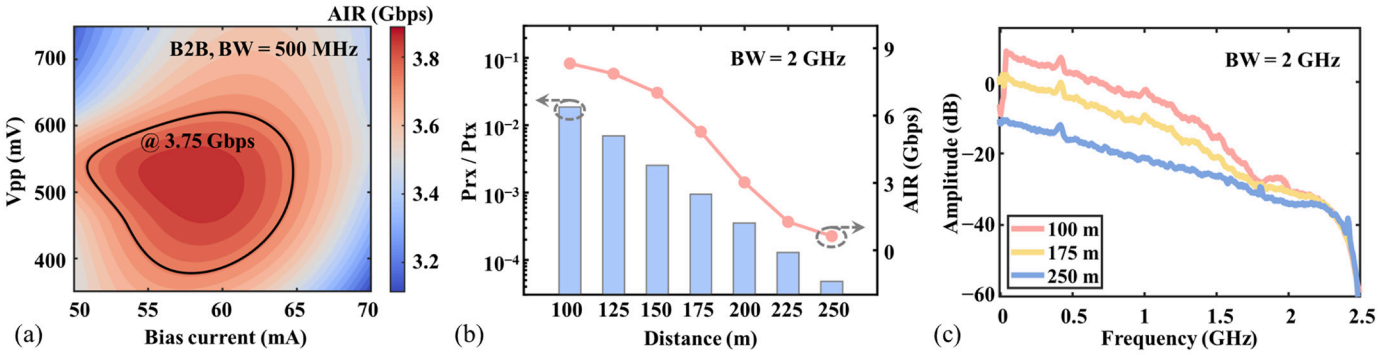

Figure 4. Achievable information rate versus (**a**) operating point and (**b**) single-hop attenuation-equivalent distance; (**c**) received signal spectra at different equivalent distances. The black contour in (**a**) indicates an AIR of 3.75 Gbps. In (**b**), the blue bars and pink line represent the received-to-transmitted power ratio (left axis) and AIR (right axis), respectively.

Subsequently, the collimated beam was transmitted through a 5 m water tank, and an optical attenuator was used to match the received optical power corresponding to longer attenuation-equivalent distances. In this work, equivalent distances are calculated using the reference diffuse attenuation coefficient of 0.0398 m^{-1} for Jerlov type-I water at 525 nm [24]. Based on this model, the corresponding P_{rx}/P_{tx} ratios for different equivalent transmission distances were calculated, as shown in the bar chart of Figure 4b. The corresponding variation in AIR with distance is also presented in Figure 4b. Figure 4c depicts the received signal spectra at equivalent distances of 100 m, 175 m, and 250 m. As the target received optical power decreases, the frequency responses of the electrical-to-optical and optical-to-electrical conversion stages, together with the SNR, jointly affect the received electrical spectrum, with more pronounced distortion in the high-frequency components. Consequently, the supported data rate and modulation order decrease significantly with increasing propagation distance.

Based on the preceding optimization, the system operating point was fixed at a Vpp of 550 mV and a bias current of 60 mA. The relay distance (RD) was initially set to 200 m. The transmitted signal was a CAP-modulated QAM-4 waveform at a symbol rate of 500 MBaud, corresponding to a data rate of 1 Gbps. We first optimized the parameters of the amplify-and-forward strategy. Figure 5a presents the BER as a function of the number of hops under different pre-equalization schemes. Neither Pre-equalization Curve 1 nor Curve 2 satisfies the 1 km transmission requirement. In contrast, the proposed spectrum-slicing pre-equalization scheme enables transmission over an attenuation-equivalent distance of 1 km. Figure 5b compares the transmitted spectra after various pre-equalization schemes and the received spectra after the second, third, and fourth hops. After four hops, the spectrum corresponding to the proposed spectrum-slicing scheme (red curve) remains the flattest among all approaches. Curve 1 (blue curve) enhances mid-frequency components

but significantly suppresses high-frequency components, whereas Curve 2 (yellow curve) leads to substantial degradation in the mid-frequency band, resulting in information loss. Figure 5c presents a performance comparison between the proposed system and a conventional point-to-point (P2P) single-aperture reception system. The results show that the single-aperture configuration supports transmission over only three hops.

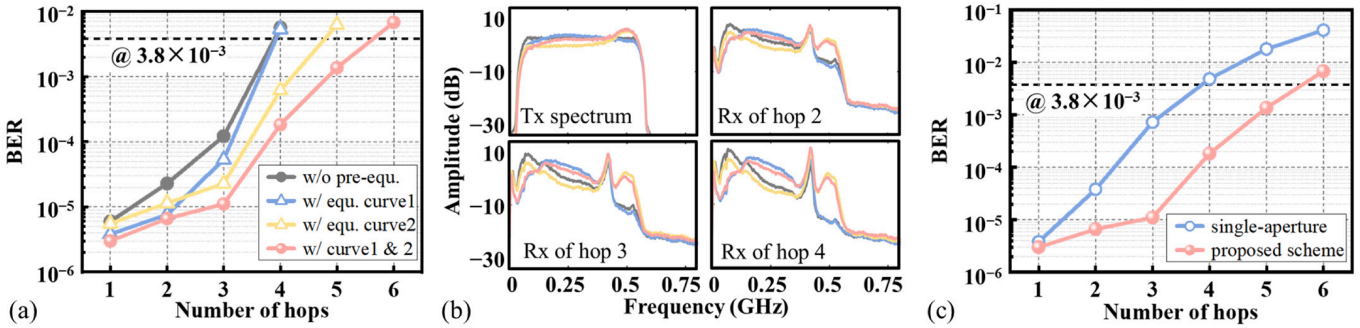

Figure 5. Results for the AF strategy: (**a**) BER and (**b**) received spectra for different pre-equalization schemes; (**c**) a performance comparison between the proposed system and a conventional P2P single-aperture reception system. The dashed horizontal lines in (**a**,**c**) indicate a BER of 3.8×10^{-3}. In (**b**), the gray, blue, yellow, and pink curves correspond to no pre-equalization, pre-equalization using curve 1, pre-equalization using curve 2, and the joint use of curves 1 and 2, respectively.

Moreover, the dual-aperture system employing LCS-PE achieves a substantially lower BER than the system relying solely on conventional time-domain equalization. Overall, the proposed AF-based relay system enables 1 Gbps QAM-4 transmission over an attenuation-equivalent distance of 1 km while satisfying the BER threshold of 3.8×10^{-3} corresponding to 7% hard-decision forward error correction (HD-FEC). This threshold is used as the end-to-end transmission criterion. It does not mean that FEC decoding is performed at relay nodes. Neither per-hop FEC decoding nor an end-to-end FEC decoding experiment is performed, and post-FEC performance is not measured. The pre-FEC BER at the final receiver is evaluated against the original transmitted data. A BER below this threshold is used to assess the feasibility of error-free transmission after FEC, subject to the selected code and decoder.

Next, ablation experiments were conducted for the DF strategy. Figure 6a illustrates the BER as a function of the number of hops for the proposed HMD-PE scheme, compared with systems without frequency-domain, time-domain, or symbol-domain equalization. The input signal, operating point, training settings, and tap numbers of the remaining equalizers were kept identical, while equalization in only one domain was removed. SC-FDE, Volterra, and LMS processing all contribute to improved reception performance.

However, as the number of hops increases, error accumulation becomes more pronounced, and the performance gap gradually widens. Figure 6b presents the constellation diagrams at the eighth hop. The first row shows constellations obtained by direct demodulation at four processing stages: (I) before equalization, (II) after frequency-domain equalization, (III) after time-domain equalization, and (IV) after symbol-domain equalization. The second row shows the constellations obtained after combining the two signals at the four stages, while the third row reports the corresponding BERs. The received waveform initially exhibits a certain phase offset. The frequency-, time-, and symbol-domain equalization stages progressively improve signal quality, further reducing BER. Therefore, combining the two polarization branches is most effective when performed after symbol-domain equalization.

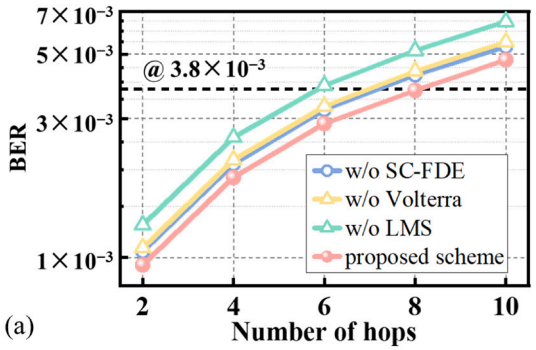

(b)

	I. Rx signal	II. After SC-FDE	III. After Volterra	IV. After LMS
Rx_H or Rx_V of I~IV				
After signal fusion at I~IV				
Final BER	4.91×10^{-3}	3.88×10^{-3}	3.86×10^{-3}	3.80×10^{-3}

Figure 6. Under the DF strategy, (**a**) performance comparison between the proposed HMD-PE scheme and systems without frequency-domain, time-domain, or symbol-domain equalization, with the remaining configuration fixed; (**b**) constellation diagrams of the received signal (Rx_H or Rx_V) obtained by direct demodulation at stages I–IV, and the final constellations and BERs after signal fusion at stages I–IV. The dashed horizontal line in (**a**) indicates a BER of 3.8×10^{-3}.

In practical systems, performance must be balanced against processing complexity [28]. The AF and DF strategies and their associated processing algorithms offer different trade-offs between performance and complexity. AF has a simpler forwarding structure, and LCS-PE has the potential for implementation using analog circuits. DF employs HMD-PE and additional per-hop processing, including multi-domain equalization, decision-making, and remodulation, to improve signal recovery at the cost of increased complexity. Depending on the application requirements, AF with LCS-PE can be selected for a shorter target transmission distance, whereas DF with HMD-PE can be selected when a longer transmission distance and higher signal fidelity are required.

4. Exploring the Attenuation-Equivalent Transmission Distance and Performance Under Disturbances

With the system using the optimized operating point and parameters, a 1 Gbps QAM-4 signal was transmitted to evaluate the nominal attenuation-equivalent distance achievable by the proposed RA-UVLC system under the tested configurations. Here, RD denotes the single-hop attenuation-equivalent distance. Figures 7 and 8 use the Jerlov type-I reference attenuation coefficient of 0.0398 m^{-1}.

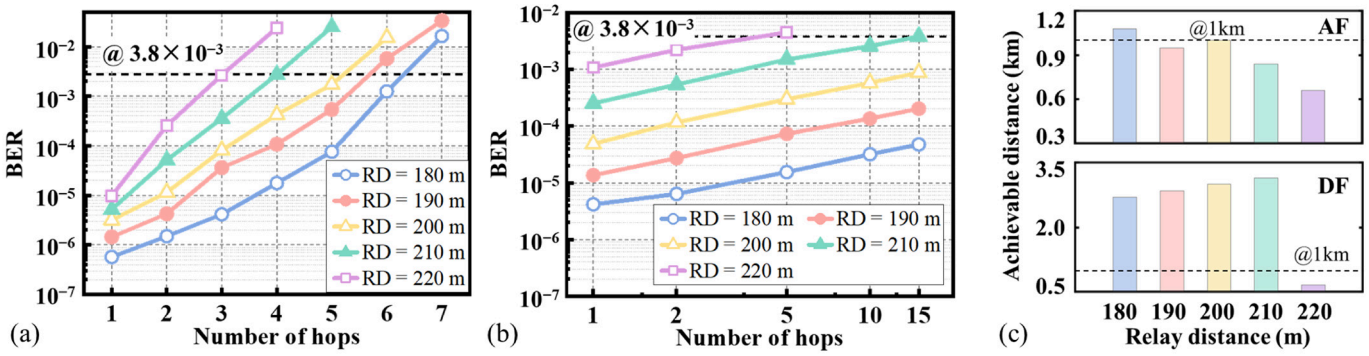

Figure 7. Measured end-to-end BER versus hop count for (**a**) AF and (**b**) DF at different single-hop attenuation-equivalent distances. (**c**) Total attenuation-equivalent distances satisfying the BER criterion within the measured hop range. The dashed horizontal lines in (**a**,**b**) indicate a BER of 3.8×10^{-3}. The dashed horizontal lines in (**c**) indicate an achievable distance of 1 km.

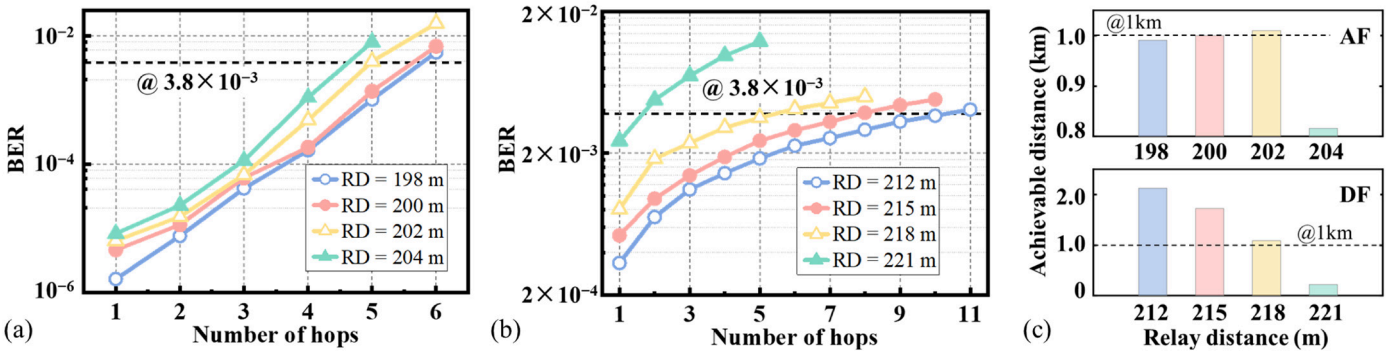

Figure 8. BER versus hop count for the (**a**) AF and (**b**) DF strategies at relay distances around 200 m; (**c**) total attenuation-equivalent distances calculated from the integer hop counts satisfying the BER threshold. The dashed horizontal lines in (**a**,**b**) indicate a BER of 3.8×10^{-3}. The dashed horizontal lines in (**c**) indicate an achievable distance of 1 km.

Figure 7 presents the BER as a function of hop count for both the AF (Figure 7a) and DF (Figure 7b) strategies under different relay distances. For the AF scheme, each hop introduces cumulative spectral attenuation that can only be partially mitigated by Zobel-network-based pre-equalization. Even with the proposed spectrum-slicing pre-equalization, perfect spectral restoration at each relay node cannot be achieved. As a result, noise and distortion accumulate progressively, leading to a rapid increase in BER over the measured hop range. In contrast, the DF scheme performs demodulation, decoding, and remodulation at every relay node. This process regenerates the transmitted waveform and mitigates the per-hop accumulation of analog noise and spectral distortion, although incorrect decisions can still affect subsequent bits. Only measured hop counts are shown in Figure 7a,b, and the connecting lines serve as visual guides. Figure 7c summarizes the attenuation-equivalent distances supported within the measured hop range. For DF configurations that remain below the BER threshold at the final measured hop, the corresponding distance is a lower bound on the attainable reach under the tested conditions. In comparison, the AF strategy exhibits non-monotonic behavior with varying relay distances. Although shorter relay distances provide higher received optical power and thus higher SNR per hop, achieving a fixed long-distance target (e.g., 1 km) may require additional relay nodes when the RD is below 200 m, leading to increased cumulative distortion and higher energy consumption. For the same forwarding scheme, node hardware, and operating conditions, the total electrical power consumption P_{total} can be calculated by summing the contributions of the transmitter ($P_{elec,tx}$), receiver ($P_{elec,rx}$), relay-processing ($P_{proc,relay}$), and destination-processing modules ($P_{proc,dest}$) as follows:

$$P_{total} = N(P_{elec,tx} + P_{elec,rx}) + (N-1)P_{proc,relay} + P_{proc,dest}. \quad (16)$$

Here, an N-hop link contains $(N-1)$ relay nodes. Under the same hardware and operating conditions, reducing the number of relays reduces the modeled total electrical power consumption. At a fixed hop count, increasing the spacing extends the equivalent coverage distance. Provided that the target BER is satisfied, greater spacing can reduce the number of relays required to cover a given equivalent distance.

Figure 8a,b present the BER as a function of hop count for RDs around 200 m under the AF and DF strategies, respectively. Figure 8c summarizes the achievable equivalent transmission distances of the two strategies. Among the tested five-hop configurations, the largest feasible relay spacings that satisfy the BER threshold and cover an attenuation-equivalent distance exceeding 1 km are 202 m and 218 m for AF and DF, respectively.

Furthermore, the received optical powers (ROPs) corresponding to the equivalent relay distances in Figures 7c and 8c are converted into equivalent distances for other reference

water types, namely Jerlov II and III, with reference attenuation coefficients of 0.0780 and 0.122 m^{-1}, respectively [24]. In descending order of ROP, the four AF configurations support 5, 5, 5, and 4 hops, whereas the corresponding DF configurations support 15, 10, 8, and 5 hops. For each water type, the single-hop equivalent distance is multiplied by the corresponding supported hop count to obtain the total equivalent distance, as shown in Figure 9.

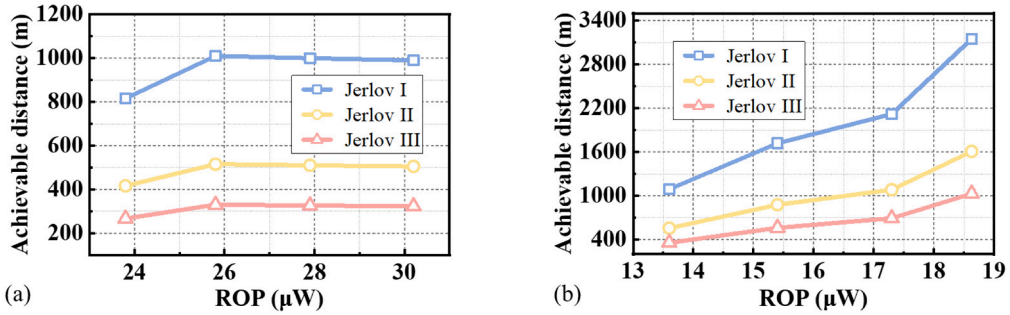

Figure 9. Total attenuation-equivalent distances for different reference water types: (**a**) AF scheme; (**b**) DF scheme.

Finally, the link is fixed at five hops to evaluate the end-to-end BER under four channel disturbance conditions: the weak (blue) and strong (red) water pump settings, and salinities of 30 ppt (yellow) and 60 ppt (green) under the weak water pump setting. The pump power, flow rate, and lift are 30 W, 4040 L/h, and 2.8 m at the strong setting, and 22 W, 2996 L/h, and 2.2 m at the weak setting, respectively. All groups use the same transmitter operating point, signal-processing parameters, and receiver-processing configuration. The labels Weak and Strong in the figure refer to the water pump settings. Figure 10a and 10b show the AF and DF results, respectively, with the horizontal axis representing the five-hop total attenuation-equivalent distance calculated using the Jerlov type-I reference coefficient. Ten measurements are taken at each point, and the mean BER is reported. The supported total equivalent distance under each disturbance condition is estimated by interpolation near the 3.8×10^{-3} threshold. These distances are then converted to Jerlov II and III equivalent distances using the corresponding reference attenuation coefficients, as shown in Figure 10c. Across the four applied disturbance conditions, DF and AF relaying support equivalent transmission distances of at least 1048 m and 974 m in Jerlov I water, 535 m and 497 m in Jerlov II water, and 342 m and 318 m in Jerlov III water, respectively. A stronger pump setting or higher salinity corresponds to a higher BER and a shorter equivalent transmission distance. Compared with the AF scheme, the DF scheme achieves a longer supported distance through per-hop signal recovery.

Building on the polarization-diversity architecture reported in [19], this study proposes and experimentally evaluates LCS-PE for AF relaying and HMD-PE for DF relaying in a UVLC system. It is worth noting that the 5 m water tank and calibrated optical attenuation reproduce the received-power conditions corresponding to longer attenuation-equivalent links, but do not reproduce beam divergence, distributed scattering, pointing errors, and turbulence over natural underwater paths of the same lengths. The pump settings and salinities define the four laboratory conditions tested. Pump settings are not equivalent to measured turbulence statistics, and salinity variation alone does not represent all seawater conditions. Scattering, pointing errors, spatial inhomogeneity, and long-term channel variability have not been independently characterized. Furthermore, LCS-PE was evaluated digitally using frequency responses calculated from circuit parameters, while HMD-PE was implemented through offline software processing. The real-time performance of an analog relay board, the overhead of a complete system, and any energy savings require

hardware measurements. Owing to limited experimental equipment, the hardware power consumption, latency, synchronization overhead, and processing cost of a complete real-time relay system have not yet been measured. Sequential acquisition, offline processing, and waveform replay preserve hop-to-hop impairment propagation, while simultaneous real-time operation of independently synchronized relay nodes remains to be evaluated. Future work will address these aspects to provide further experimental evidence for practical relay-assisted UVLC systems.

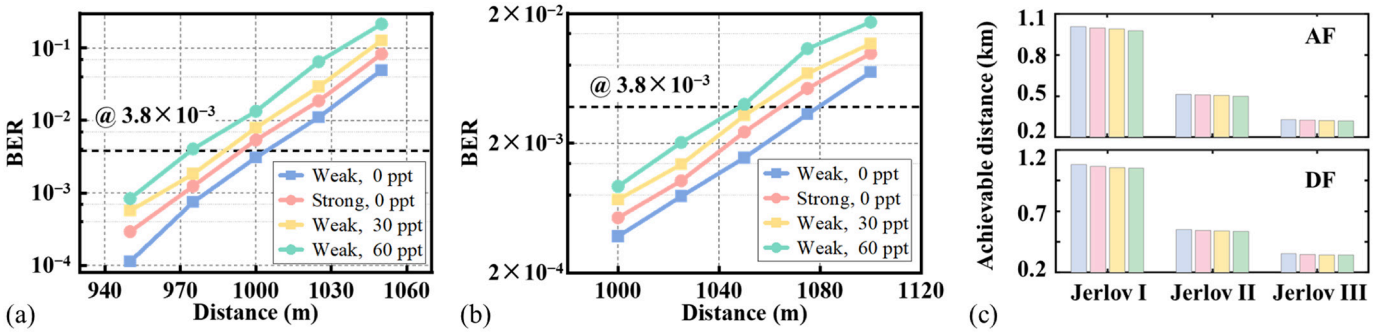

Figure 10. Five-hop transmission results under different channel disturbance conditions: mean end-to-end BER for (**a**) AF and (**b**) DF using the Jerlov type-I reference attenuation coefficient; (**c**) supported distances obtained by interpolation of the mean BER curves at the threshold, together with the converted total equivalent distances for Jerlov II and III. Weak and Strong denote the weak and strong water pump settings, respectively. The dashed horizontal lines in (**a**,**b**) indicate a BER of 3.8×10^{-3}. The blue, pink, yellow, and green bars in (**c**) correspond to the "Weak, 0 ppt", "Strong, 0 ppt", "Weak, 30 ppt", and "Weak, 60 ppt" conditions, respectively.

5. Conclusions

In this work, a relay-assisted underwater visible light communication system based on a green laser was experimentally demonstrated, and the feasibility and relative performance of amplify-and-forward and decode-and-forward relay strategies were systematically evaluated. To mitigate high-frequency roll-off and signal distortion arising from device noise and bandwidth limitations, a joint hierarchical equalization scheme was proposed, including a lightweight cascaded spectral pre-equalization scheme for amplify-and-forward relaying and a hierarchical multi-domain post-equalization scheme for decode-and-forward relaying. Transmission through a 5 m water tank with equivalent attenuation imposed by NDFs enabled both AF and DF to achieve a data rate of 1 Gbps over an attenuation-equivalent distance of 1 km. The end-to-end BER and supported equivalent distances of the two strategies were further compared under different water pump-induced disturbance levels and salinity conditions. AF provides a simpler forwarding structure, whereas DF achieves better signal recovery through additional per-hop processing. These results provide experimental evidence for relay scheme selection.

Author Contributions: Conceptualization, Z.L. (Zhilan Lu) and N.C.; methodology, Z.L. (Zhilan Lu), F.L. and F.D.; software, Z.L. (Zhilan Lu), F.L., F.D., and Z.X.; validation, F.L., F.D. and Z.X.; formal analysis, Z.L. (Zhilan Lu), F.L. and F.D.; investigation, Z.L. (Zhilan Lu), F.L. and F.D.; resources, Z.L. (Ziwei Li), F.B., C.S., J.Z. and N.C.; data curation, Z.L. (Zhilan Lu), F.L. and F.D.; writing—original draft preparation, Z.L. (Zhilan Lu); writing—review and editing, Z.L. (Zhilan Lu), Z.L. (Ziwei Li), F.B., C.S., J.Z. and N.C.; visualization, Z.L. (Zhilan Lu); supervision, N.C. All authors have read and agreed to the published version of the manuscript.

Funding: This research was funded by the Natural Science Foundation of China, under Grant No. 62525102.

Data Availability Statement: The original contributions presented in the study are included in the article; further inquiries can be directed to the corresponding author.

Conflicts of Interest: The authors declare no conflicts of interest.

Abbreviations

The following abbreviations are used in this manuscript:

VLC	Visible Light Communication
UVLC	Underwater Visible Light Communication
RA-UVLC	Relay-Assisted Underwater Visible Light Communication
AF	Amplify-And-Forward
DF	Decode-And-Forward
JHES	Joint Hierarchical Equalization Scheme
LCS-PE	Lightweight Cascaded Spectral Pre-Equalization
HMD-PE	Hierarchical Multi-Domain Post-Equalization
RD	Relay Distance

References

1. You, X.; Wang, C.-X.; Huang, J.; Gao, X.; Zhang, Z.; Wang, M.; Huang, Y.; Zhang, C.; Jiang, Y.; Wang, J.; et al. Towards 6G Wireless Communication Networks: Vision, Enabling Technologies, and New Paradigm Shifts. *Sci. China Inf. Sci.* **2020**, *64*, 110301. [CrossRef]
2. Tataria, H.; Shafi, M.; Molisch, A.F.; Dohler, M.; Sjöland, H.; Tufvesson, F. 6G Wireless Systems: Vision, Requirements, Challenges, Insights, and Opportunities. *Proc. IEEE* **2021**, *109*, 1166–1199. [CrossRef]
3. Chi, N.; Zhou, Y.; Wei, Y.; Hu, F. Visible Light Communication in 6G: Advances, Challenges, and Prospects. *IEEE Veh. Technol. Mag.* **2020**, *15*, 93–102. [CrossRef]
4. Chi, N.; Niu, W.; Zhou, Y.; Wang, J.; Chen, H.; He, Z.; Li, J.; Xu, Z.; Lin, X.; Luo, Z.; et al. Enabling Technologies to Achieve Beyond 500 Gbps Optical Intra-Connects Based on WDM Visible Light Laser Communication. *J. Light. Technol.* **2025**, *43*, 1843–1854. [CrossRef]
5. Ghassemlooy, Z.; Arnon, S.; Uysal, M.; Xu, Z.; Cheng, J. Emerging Optical Wireless Communications-Advances and Challenges. *IEEE J. Sel. Areas Commun.* **2015**, *33*, 1738–1749. [CrossRef]
6. Saeed, N.; Celik, A.; Al-Naffouri, T.Y.; Alouini, M.-S. Underwater Optical Wireless Communications, Networking, and Localization: A Survey. *Ad Hoc Netw.* **2019**, *94*, 101935. [CrossRef]
7. Kaushal, H.; Kaddoum, G. Underwater Optical Wireless Communication. *IEEE Access* **2016**, *4*, 1518–1547. [CrossRef]
8. Li, F.; Zhang, H.; Lu, Z.; Yao, L.; Wei, Y.; Li, Z.; Bao, F.; Zhang, J.; Zhou, Y.; Chi, N. Unsupervised Learning Enabled Label-Free Single-Pixel Imaging for Resilient Information Transmission through Unknown Dynamic Scattering Media. *Opto-Electron. Adv.* **2025**, *8*, 250013. [CrossRef]
9. Hu, J.; Jia, H.; Gu, Z.; Yang, Z.; Yu, S.; Xia, C.; Zhang, J.; Li, Z.; Zhou, Y.; Shi, J.; et al. Investigation on Large Modulation Bandwidth InGaN-Based Blue Laser Diodes. *Opt. Laser Technol.* **2025**, *185*, 112601. [CrossRef]
10. Jia, H.; Hu, J.; Xu, Z.; Gu, Z.; Yang, Z.; Li, Z.; Zhou, Y.; Shi, J.; Li, Z.; Zhang, J.; et al. High-Speed Blue Laser Diodes with InGaN Quantum Barrier for Beyond 36 Gbps Visible Light Communications. *Laser Photonics Rev.* **2025**, *19*, 2401751. [CrossRef]
11. Cao, R.; Yang, L.; Qu, F. On the Capacity and System Design of Relay-Aided Underwater Acoustic Communications. In *Proceedings of the 2010 IEEE Wireless Communication and Networking Conference*; IEEE: New York, NY, USA, 2010; pp. 1–6.
12. Fei, C.; Wang, Y.; Du, J.; Chen, R.; Lv, N.; Zhang, G.; Tian, J.; Hong, X.; He, S. 100-m/3-Gbps Underwater Wireless Optical Transmission Using a Wideband Photomultiplier Tube (PMT). *Opt. Express OE* **2022**, *30*, 2326–2337. [CrossRef] [PubMed]
13. Lu, C.; Wang, J.; Li, S.; Xu, Z. 60m/2.5Gbps Underwater Optical Wireless Communication with NRZ-OOK Modulation and Digital Nonlinear Equalization. In *Proceedings of the 2019 Conference on Lasers and Electro-Optics (CLEO)*; IEEE: New York, NY, USA, 2019; pp. 1–2.
14. Jamali, M.V.; Akhoundi, F.; Salehi, J.A. Performance Characterization of Relay-Assisted Wireless Optical CDMA Networks in Turbulent Underwater Channel. *IEEE Trans. Wirel. Commun.* **2016**, *15*, 4104–4116. [CrossRef]
15. Furqan Ali, M.; Ponnimbaduge Perera, T.D.; Sergeevich, V.S.; Arbid Irfan, S.; Ekaterina Viktorovna, U.; Zhang, W.; Camponogara, Â.; Jayakody, D.N.K. Selection Relay-Based RF-VLC Underwater Communication System. In *Machine Learning, Deep Learning and Computational Intelligence for Wireless Communication*; Gopi, E.S., Ed.; Springer: Singapore, 2021; pp. 177–192.
16. Luo, H.; Wang, X.; Bu, F.; Yang, Y.; Ruby, R.; Wu, K. Underwater Real-Time Video Transmission via Wireless Optical Channels With Swarms of AUVs. *IEEE Trans. Veh. Technol.* **2023**, *72*, 14688–14703. [CrossRef]

17. Jiang, Y.; Li, Y.; Zhang, X.; Ju, M.; Huang, P. Outage Performance Analysis for Relay-Assisted UWOC Systems over GGD Weak Turbulence with Nonzero Boresight Pointing Errors. *Phys. Commun.* **2023**, *58*, 102017. [CrossRef]
18. Salman, M.; Bolboli, J.; Naik, R.P.; Chung, W.-Y. Aqua-Sense: Relay-Based Underwater Optical Wireless Communication for IoUT Monitoring. *IEEE Open J. Commun. Soc.* **2024**, *5*, 1358–1375. [CrossRef]
19. Lu, Z.; Li, F.; Cai, J.; Lin, X.; Xu, Z.; Zhou, Y.; Shi, J.; Shen, C.; Li, Z.; Zhang, J.; et al. Turbulence Resistant Dual-Aperture Receiver with a Sparse Dual-Polarization Triple-Branch Network in Underwater Visible Light Communication. *J. Light. Technol.* **2025**, *43*, 7663–7675. [CrossRef]
20. Huang, X.; Chen, S.; Wang, Z.; Shi, J.; Wang, Y.; Xiao, J.; Chi, N. 2.0-Gb/s Visible Light Link Based on Adaptive Bit Allocation OFDM of a Single Phosphorescent White LED. *IEEE Photonics J.* **2015**, *7*, 7904008. [CrossRef]
21. Ab Aziz, S.H.; Nor, N.A.M.; Ghassemlooy, Z.; Zvanovec, S.; Bohata, J. Investigation of Hardware Equalizer Based on a Bridged-T Network for High-Speed VLC. In *Proceedings of the 2024 14th International Symposium on Communication Systems, Networks and Digital Signal Processing (CSNDSP)*; IEEE: New York, NY, USA, 2024; pp. 256–261.
22. Huang, X.; Shi, J.; Li, J.; Wang, Y.; Chi, N. A Gb/s VLC Transmission Using Hardware Preequalization Circuit. *IEEE Photonics Technol. Lett.* **2015**, *27*, 1915–1918. [CrossRef]
23. Azim, A.W.; Rahman, T.; Bazzi, A.; Uysal, M.; Chafii, M. Timing Synchronization and Channel Estimation for DCO-OFDM in VLC Systems. In *Proceedings of the 2025 IEEE 36th International Symposium on Personal, Indoor and Mobile Radio Communications (PIMRC)*; IEEE: New York, NY, USA, 2025; pp. 1–6.
24. Solonenko, M.G.; Mobley, C.D. Inherent Optical Properties of Jerlov Water Types. *Appl. Opt.* **2015**, *54*, 5392–5401. [CrossRef] [PubMed]
25. Hu, J.; Guo, Z.; Shi, J.; Jiang, X.; Chen, Q.; Chen, H.; He, Z.; Song, Q.; Xiao, S.; Yu, S.; et al. A Metasurface-Based Full-Color Circular Auto-Focusing Airy Beam Transmitter for Stable High-Speed Underwater Wireless Optical Communications. *Nat. Commun.* **2024**, *15*, 2944. [CrossRef] [PubMed]
26. Lin, X.; Zhang, H.; Lu, Z.; Luo, Z.; Shen, C.; Shi, J.; Zhang, J.; Li, Z.; Chen, H.; He, Z.; et al. 519.21Gbps Optical Interconnect Using 50-Channel Pre-Equalized WDM Visible Light Laser Communication System. In *Proceedings of the 2024 Optical Fiber Communications Conference and Exhibition (OFC)*; Optica Publishing Group: Washington, DC, USA, 2024; pp. 1–3.
27. Zhou, Y.; Lin, X.; Xu, Z.; Lu, Z.; Huang, Y.; Luo, Z.; Zhang, H.; Sun, L.; Ye, J.; He, Z.; et al. Beyond 600Gbps Optical Interconnect Utilizing Wavelength Division Multiplexed Visible Light Laser Communication [Invited]. *Chin. Opt. Lett.* **2025**, *23*, 050002. [CrossRef]
28. Xian, Y.; Ding, X.; Gao, X.; Li, G.; Yang, K.; An, J. A Low-Complexity APSK Iterative Receiver With Convergence- and Oscillation-Aware Early Termination Strategies. *IEEE Trans. Veh. Technol.* **2026**, 1–15. [CrossRef]

Disclaimer/Publisher's Note: The statements, opinions and data contained in all publications are solely those of the individual author(s) and contributor(s) and not of MDPI and/or the editor(s). MDPI and/or the editor(s) disclaim responsibility for any injury to people or property resulting from any ideas, methods, instructions or products referred to in the content.